TITLE: A zebrafish xenotransplant model of anaplastic thyroid cancer to study the tumor microenvironment and innate immune cell interactions *in vivo*.

AUTHORS: Cassia Michael[1], Antonio Di Cristofano[1,2,5,6], and Sofia de Oliveira[1,3-6]

[1]Department of Developmental and Molecular Biology, Albert Einstein College of Medicine, Bronx, NY, USA.
[2]Department of Medicine (Oncology), Albert Einstein College of Medicine, Bronx, NY, USA.
[3]Department of Medicine (Hepatology), Albert Einstein College of Medicine, Bronx, NY, USA.
[4]Marion Bessin Liver Research Center, Albert Einstein College of Medicine and Montefiore Medical Center, Bronx, NY, USA.
[5]Montefiore-Einstein Cancer Research Center, Albert Einstein College of Medicine, Bronx, NY, USA.
[6]Cancer Dormancy Tumor Microenvironment Institute, Albert Einstein College of Medicine, Bronx, NY, USA.

CORRESPONDING AUTHOR: Sofia de Oliveira, sofia.deoliveira@einsteinmed.edu
ORCID: 0000-0003-0893-111X

KEY WORDS: Zebrafish, microscopy, tumor microenvironment, neutrophils, xenotransplant

SUMMARY STATEMENT: Anaplastic thyroid cancer xenotransplant model in zebrafish larvae to study thyroid cancer tumorigenesis and tumor microenvironment. Using confocal microscopy to understand cell cycle progression, interactions with the innate immune system, and test therapeutic compounds in vivo.

Abstract

Anaplastic thyroid cancer (ATC) is a rare malignant subtype of thyroid cancer. While ATC is rare it accounts for a disproportionately high number of thyroid cancer-related deaths. Here we developed an ATC xenotransplant model in zebrafish larvae, where we can study tumorigenesis and therapeutic response in vivo. Using both mouse (T4888M) and human (C643) derived fluorescently labeled ATC cell lines we show these cell lines display different engraftment rates, mass volume, proliferation, and angiogenic potential. Next, using a PIP-FUCCI reporter to track proliferation *in-vivo* we observed cells in each phase of the cell cycle. Additionally, we performed long-term non-invasive intravital microscopy over 72 hours to understand cellular dynamics in the tumor microenvironment at the single cell level. Lastly, we tested a well-known mTOR inhibitor to show our model could be used as an effective screening platform for new therapeutic compounds. Altogether, we show that zebrafish xenotransplants make a great model to study thyroid carcinogenesis and the tumor microenvironment, while also being a suitable model to test new therapeutics *in vivo*.

Introduction

Anaplastic thyroid cancer (ATC) is a rare, undifferentiated, and highly aggressive form of thyroid cancer associated with poor prognosis. Although its incidence is low (i.e., ~3% of all thyroid cancer cases), it accounts for nearly half of all thyroid cancer-related deaths, as a consequence of its unresponsiveness to current treatment options (1). Since many aspects of the biology of these tumors are still obscure, we decided to develop a novel ATC xenotransplant model in zebrafish larvae that allows to study thyroid cancer biology and therapeutic response in vivo, including evaluation of the tumor architecture, composition and dynamics of the tumor microenvironment, and the visualization of drug effects in vivo.

Zebrafish are a powerful non-mammalian vertebrate model to study many human diseases, including cancer. Xenotransplants in zebrafish larvae are a well-established model for multiple cancers, such as colorectal and breast, that have gained popularity for their fast development, high fecundity, easy genetic manipulation and *in vivo* tractability (2, 3, 4). But perhaps their biggest asset is optical transparency, which allows for long-term non-invasive live imaging of the tumor microenvironment, and the ability to perform robust high throughput drug and genetic screenings (2). Importantly, they offer a shorter experimental timeline and do not have a fully developed adaptive immune system until 2-3 weeks post fertilization, with lymphoid lineage appearing by 10 days post-fertilization (5). This allows for the use of an immune competent model and a unique opportunity to study the interaction between cancer cells and innate immune cells, and further explore mechanisms of innate immune evasion (6). While ATC

67 xenotransplants in zebrafish have been previously reported, a full characterization of the model
68 has never been done (7).
69
70 Here, we injected fluorescently labeled mouse and human-derived ATC cell lines into the
71 perivitelline space (PVS) of zebrafish larvae at 2 days post fertilization (dpf) (3) and tracked their
72 engraftment rate, mass volume, proliferation and angiogenic potential. Furthermore, we tested
73 AZD2014, a well-known mTOR inhibitor, to validate its ability to arrest cells in our model.
74 Altogether, our results show that zebrafish larvae xenotransplants are a promising *in vivo*
75 model to investigate ATC tumor microenvironment, tumorigenesis, and explore new
76 therapeutics.
77
78 **Results**
79
80 **ATC cell lines engraft in zebrafish larvae at different rates.**
81
82 Zebrafish are a powerful and dynamic model organism to study cancer biology (6). To test if
83 anaplastic thyroid cancer (ATC) cell lines can engraft 2 days post fertilization (dpf) zebrafish
84 larvae, were injected with mouse N794, T1903, T1860, N2773, N2933, and T4888M and human
85 ACT1, BHT101, ASH3, and C643 ATC cell lines and followed masses up to 4 days post injection
86 (dpi) (Figure 1A). Around 300-500 cancer cells were injected into the perivitelline space (PVS),
87 the pocket between the zebrafish yolk and the outer dermal membrane (Figure 1B), mimicking
88 a subcutaneous injection in mouse model. Next, we explored the engraftment potential of the
89 different ATC cell lines (Figure 1C). At 4dpi, we observed that mouse cell lines have similar
90 engraftment potential, with an engraftment rate ranging between 70%-100 (N794=87%,
91 T1903=69%, T1860=83%, N2773=98%, N2933=60% and T4888M=98%) , while human cell lines
92 have engraftment rates between 40-60% (ACT1=57%, BHT101=60%, ASH3=42% and C643=64%)
93 (Figure 1C and D). Histopathological analysis of the zebrafish tumor masses derived from the
94 T4888M cell line shows that they have similar morphological features as observed previously in
95 mice (Figure 1E-G). In addition, we observed two major characteristics of ATC thyroid cancer in
96 both T4888M and C643 zebrafish masses, which are spindle cell/nuclear spindle formation and
97 pleomorphic cells (11). Spindle cell and nuclear spindle formation can be identified by their
98 elongated and thinner morphology (Figure 1E'-G', 1L'), while pleomorphic cells were identified
99 by their abnormal shape and variation amongst cells (Figure 1E'-G', 1J'-L'). These findings
100 suggest that both human and mouse ATC cell lines can engraft in zebrafish larvae and that
101 masses preserve major ATC histological features.
102
103 **T4888M and C643 ATC cell lines display different growth and proliferation rates.**
104

105 For the remainder of the experiments, we utilized the two cell lines with higher engraftment
106 rates, the mouse line T4888M and the human line C643. To further characterize the ATC
107 xenografts, we next tested if both human and mouse lines could grow and proliferate in the
108 zebrafish. Thus, we performed non-invasive intravital confocal microscopy of xenografts at 1
109 and 4dpi and after IMARIS imaging analysis we observed that the T4888M cell line mass volume
110 significantly increased over the 4 days while a reduction was observed for the C643 cell line
111 (Figure 2A,2B). Additionally, we assessed the proliferation of larvae xenografts for both cell
112 lines by EDU (5-ethynyl-2'deoxyuridine) incorporation over 4 hours. Not surprisingly, we
113 observed a higher density and number of EDU positive cells in the T4888M xenograft masses in
114 comparison to the C643 (Figure 2E,2F). Overall, our results show that both mouse and human
115 lines can proliferate in the zebrafish larvae, with mouse ATC line demonstrating higher growth
116 and proliferative rates, while in human cells the proliferative rate is not sufficient to overcome
117 cell loss.
118
119 **T4888M ATC xenotransplants display high angiogenic ability.**
120
121 An important feature that supports cancer growth and proliferation is angiogenesis (12). To
122 understand why there are such large differences in mass volume and proliferation between the
123 T4888M and C643 cell lines, we looked at the ability of both cell lines to recruit vessels to the
124 mass using a transgenic zebrafish line, Tg(Fli1:eGFP) that labels vasculature with GFP (13). At
125 4dpi, we observed that the T4888M cell line has a dramatically higher angiogenic potential,
126 with xenografts displaying highly vascularized masses compared to the C643 cells (Figure 3A-D).
127 The T4888M cell line forms a dense organization of vessels that infiltrate the mass, while the
128 C643 masses recruit almost no vessels to the mass (Movie S1,S2). Correlation analysis shows
129 that increased vessel volume is correlated to increased mass volume for the T4888M xenografts
130 (Figure 3E). However, for the C643 xenografts, vessel volume is not correlated to mass volume,
131 which is consistent with the larger C643 masses we observed that lack vessel infiltration (Figure
132 3F). Together, these findings suggest that T4888M has an extensive angiogenic potential
133 compared to C643 that may be contributing to the observed higher survival, proliferation and
134 growth rates.
135
136 **In vivo visualization of T4888M cell cycle using the PIP-FUCCI reporter.**
137
138 To further understand the proliferative capacity and cellular dynamics of the T4888M cell line,
139 we incorporated a PIP-FUCCI reporter into the cells. This reporter allowed us to delineate
140 various phases of the cell cycle, optimizing our ability to do long-term in vivo imaging at the
141 single cell level (14). This two-colored reporter expresses GFP when cells are in G1 and as they
142 transition to late S phase it expresses mCherry. When cells are in G2/M both GFP and mCherry

are expressed, allowing for colocalization of signal to detect these cells (14). Again, using non-invasive confocal microscopy followed by IMARIS imaging analysis we determined which phase of the cell cycle cells were at 4dpi (Figure 4A). At this timepoint we observe the highest number of cells to be in G1 and the second highest to be in late S-phase (Figure 4B). This is also consistent when the number of cells in each phase is normalized by the total number of cells in each mass (Figure 4C). Next, to investigate the cell division dynamics on T4888 masses, we performed long term time-lapse microscopy for over 48 hours and observed that these masses maintain their ability to proliferate (Figure 4D-E).

T4888M ATC cell line responds to cell cycle inhibitors.

To understand if our model could be used for preclinical screenings, we performed a proof-of-principle experiment using the well-known mTOR inhibitor, AZD2014. Using the PIP-FUCCI reporter coupled with non-invasive confocal microscopy and image analysis we observed that the inhibitor significantly reduced the total number of cells in each mass (Figure 5A, 5B). When looking more closely at the individual cell phases, we observed that the AZD2014 compound causes a reduction of cells in late S and an increase in cells in G1, when compared to the DMSO control (Figure 5C). As expected, the treatment did not have a significant impact on cells in G2/M phase. Lastly, we looked at neutrophil infiltration into T4888 ATC masses (Figure 5D). We observed neutrophils to infiltrate these masses and after treatment with AZD2014 we observed a reduction in the total number of neutrophils, when compared to the DMSO control (Figure 5E & 5F). This data suggest that our model is a viable and powerful system that can be used to screen compounds that impact ATC tumorigenesis. Additionally, it can be used to study the impact of the innate immune cells on ATC tumorigenesis and the tumor microenvironment.

Discussion

Anaplastic thyroid cancer (ATC) is the deadliest and most aggressive form of thyroid cancer, with an average survival of 9 months after diagnosis. Although ATC has a low incidence rate, its highly aggressive nature makes it resistant to many already approved therapeutics, generating a need for new and efficient approaches (15). While ATC zebrafish xenotransplant models have been previously reported (7), here we developed and characterized a new in vivo model that allows visualization of cellular dynamics and tumorigenesis non-invasively at the single cell level. Additionally, our model provides an approach for the identification of new small molecules and actionable targets that can effectively inhibit tumor progression.

The ability to perform whole animal non-invasive live imaging, easy genetic manipulation and cell trackability have made zebrafish an extremely powerful system to study cancer biology

181 both using xenotransplants or tumor-induced models (16). As a small vertebrate with more
182 than 80% homology in genes related to human disease, zebrafish can be modulated to further
183 understand cancer related pathways, through transgenesis, gene specific knockouts or by
184 modulating cell responsiveness to the tumor microenvironment (17). Zebrafish larval xenografts
185 have proven to be a powerful model with many advantages over traditional xenograft models.
186 Reduced size scale and time make this a unique system to investigate cancer biology and tumor
187 microenvironment, perform medium-high throughput drug screenings, and explore
188 personalized medicine approaches (2, 17).
189
190 Our findings show that zebrafish larvae are a viable model to study thyroid carcinogenesis and
191 the ATC tumor microenvironment *in vivo*. We found that different mouse and human ATC lines
192 successfully engraft, with rates ranging from 40 to 100%. Zebrafish thyroid xenograft models
193 effectively display many hallmark characteristics of tumor progression and ATC histopathology.
194 Spindle cell and nuclear spindle cell formation are the most abundant cytological features seen
195 in ATC cells, identified by their long slender shape that assemble in an almost striated pattern
196 (11). Pleomorphic cells are the second most common cytological feature found in ATC tumors
197 characterized by abnormal cell and nuclear variation (11).Both of these features were observed
198 in xenograft masses, indicating that ATC cells are maintaining their original features. While it's
199 important for xenotransplants to maintain these characteristics, it is of equal importance for
200 them to sustain proliferative capabilities. One of the most fundamental traits of cancer cells is
201 their ability to proliferate uncontrollably. Here, we show that after cell transplantation both the
202 T4888M and the C643 cancer cells maintain their ability to proliferate in zebrafish larvae in a
203 period over 4 days, however T488M displays a much higher proliferation rate compared to
204 C643. Another hallmark of tumor progression is the ability to recruit vasculature to the mass
205 (12). Tumor masses require recruitment of vasculature to continue growing. Proper vasculature
206 provides oxygen, nutrients, and removes waste from masses. Additionally, it facilitates the
207 dissemination and metastasis of cancer cells to distant sites by access to circulation (18). We
208 observe at 4 dpi that the T4888M xenografts display a high angiogenic rate that positively
209 correlates with mass size, contrary to the C643 line, which shows a low angiogenic potential,
210 recruiting almost no vessels to the masses. This difference in angiogenic potential between
211 these two lines can partially explain the lower proliferative rate and mass growth found in
212 C643. Indeed, the C643 line compared to other ATC cell lines produces lower amounts of IL8,
213 which is a powerful pro-angiogenic factor including in zebrafish model (19, 20). Surprisingly,
214 some C643 xenografts developed big masses with low to no vessel formation within the
215 masses, suggesting that this cell line can grow at some extent without the presence of tumor
216 vasculature, at least in the zebrafish larvae model. It is important to note that some ATC cell
217 lines do not engraft as well as others; which can potentially be explained by mechanism of

218 innate immune cell evasion, as observed for models of colon cancer: future experiments will
219 provide more insight into these differences and mechanism in ATC (3).
220
221 Next, we looked at T4888M cell cycle dynamics at the single cell level using a PIP-FUCCI
222 reporter. The PIP-FUCCI reporter delineates each phase of the cell cycle, which gave us a better
223 understanding of T4888M ability to proliferative *in vivo*. Using this tool associated with long
224 term time-lapse confocal microscopy, we observed that T4888M injected cells engage in a
225 dynamic proliferative stage, as shown by EDU incorporation at 4dpi. Next, as a proof of
226 principle, we tested the effect of on proliferation of AZD2014 a dual mTORC1 and mTORC2
227 inhibitor which is expected to inhibit T4888M cells, which are driven by a mutation in *Pten* that
228 activates the PI3K/AKT/mTOR signaling pathway. We observe, at 3 days post treatment with
229 AZD2014, a reduction in the number of proliferating cells and an increase in the number of cells
230 in G1, suggesting the cells are undergoing arrest. Additionally, we were able to observe that
231 ATC masses are heavily infiltrated with neutrophils, without changes in infiltration density upon
232 treatment with AZD2014. ATC cells may be releasing inflammatory chemokine signals calling
233 neutrophils to the mass, such as CXCL1 or CXCL8 and may be interesting targets for future work
234 (21). Nevertheless, the subtype of neutrophils that are present before and after treatment
235 might be different. Neutrophils play a dual role in cancer depending on the tumor
236 microenvironment. They can be pro-tumor supporting cell cycle progression and metastasis.
237 But can also acquire a cytotoxic anti-tumor role. Recently, it has been shown neutrophils
238 immune checkpoint (IC) therapy activate neutrophils to clear tumor antigen escape variants
239 and elicit neutrophils to acquire an interferon signature that is essential for successful response
240 to therapy (22). Our zebrafish ATC model will be a valuable tool to help better understand the
241 pathophysiological role these innate immune cells are playing in ATC and if they can be
242 explored as a way to help eradicate ATC.
243
244 Overall our work provides a new powerful *in vivo* platform that allows for fast and highly
245 sensitive assays that can be used to better understand ATC biology, tumor microenvironment,
246 and therapeutic efficiency, as well as explore small molecule drug screening (3). In addition,
247 zebrafish xenografts could represent the initial step for preclinical screening before moving to a
248 more expensive model, helping to expedite studies from bench to bedside, and potentially to
249 personalized medicine (5). Taken together, our data suggests that zebrafish are a promising
250 model to study ATC cancer biology in particular when using cell lines derived from relevant
251 genetically engineered mouse models.
252
253 **Materials and Methods**
254
255 **Zebrafish general procedures and lines**

256 All protocols using zebrafish in this study were approved by the Albert Einstein College of
257 Medicine Institutional Animal Care and Use Committees (IACUC). For all experiments, larvae
258 were anesthetized in E3 (embryo medium) without methylene blue containing 0.16 mg/ml
259 tricane (MS22/ethyl3-aminobenzoate - Sigma Aldrich). Transgenic line expressing BFP under the
260 lyzC promoter in the membrane of neutrophils Tg(lyzC:BFP)^{zf217Tg} and transgenic line expressing
261 eGFP under the fli1 promoter of endothelial cells Tg(fli1:EGFP)^{y1Tg} were used in this study (4).
262 The mutant line Casper$^{Roya9;mitfaw2}$ was also used in this study (5).
263
264 **ATC Cell line maintenance**
265 All cell lines in this study (Table 1) were maintained at 37°C with 5% CO2 in RPMI1640 (human
266 cells) or DMEM (mouse cells) with 10%FBS. Cell line identity was confirmed by STS profiling as
267 well as by amplifying and sequencing genomic fragments for known mutations (7-8).
268
269 **Fluorescently labeled cell lines lines**
270 Cells were transduced with lentiviral constructs encoding Luciferase and tdTomato (Addgene
271 #72486) or the cell cycle marker PIP-FUCCI (Addgene #118616). Transduced cells were selected
272 by FACS sorting.
273
274 **Cell line preparation and injection**
275 All cell lines used in this study were allowed to expand for 1-2 weeks before harvesting. At 80%
276 of confluence, cells were trypsinized, collected, and resuspended in RPMI1640 without EDTA. A
277 cell suspension at 0.25-0.5 x 10^6 cells/μL was prepared for injection. Zebrafish larvae
278 xenotransplants injections were performed as previously reported, with some brief alterations
279 (8). At 2dpf, larvae were collected and dechorionated using forceps, anesthetized in 0.016%
280 tricaine (MS-222), and 300-500 cells were injected into the perivitelline space (PVS). Fish were
281 transferred to a plate with E3 to recover for 15-20 minutes before being placed in a 34°C
282 incubator for the remainder of the experiment. At 1dpi the xenotransplant larvae were
283 screened for the presence of cancer cells in the PVS, and larvae without cells or larvae that
284 were improperly injected were discarded.
285
286 **I*n-vivo* live imaging**
287 At 1dpi and or 3dpi larvae were anesthetized in 0.016% tricaine and used for non-invasive live
288 imaging at stereomicroscope or spinning disk confocal. All imaging was performed using a
289 zWEDGI device, designed to orient and entrap zebrafish for long-term time-lapse microscopy
290 (6). For long-term imaging, 2% low melting point agarose (Sigma-Aldrich) was placed at loading
291 chamber of the ZWEDGI to retain larvae in the correct orientation. Additional 0.016% tricaine
292 was added as needed over the course of 72-hour imaging. Images were all acquired with live
293 larvae apart from the EDU assay. Images were acquired on a spinning disk confocal microscope

294 (CSU-W, Yokogawa) with a confocal scanhead on a Zeiss Observer Z.1 inverted microscope
295 equipped with Photometrics Evolve EMCCD camera, and an EC Plan Neofluar NA 0.5/20x air and
296 0.5/40x air objective, z-stacks, 1.5 μm optical sections. For time-lapse movies, images were
297 taken with a NA 0.5/40x air objective, z-stacks, 1.5 μm optical sections, every 15 minutes for 72
298 hours.
299
300 **Drug treatments**
301 At 1 dpi zebrafish xenotransplants were screened for masses and randomly distributed into
302 treatment groups with 30 larvae per condition, 0.1% DMSO control or 1μM AZD2014
303 (Vistusertib). Larvae were treated for 3 days in 6-well plates and treatments were refreshed
304 daily (3).
305
306 **Histology**
307 After live imaging, larvae were euthanized in 0.4% tricaine and fixed in 2 ml round bottom
308 tubes with 10% formalin. Larvae in 10% formalin were mounted in 2% low melting point
309 agarose and positioned flat on their side. The cassettes were the processed by Einstein
310 Histopathology Service, embedded in parafilm, sectioned, and stained with H&E. Slides were
311 digitally scanned by Einstein's Analytical Imaging Facility on 3D HISTECH P250 High-Capacity
312 Slide Scanner.
313
314 **EDU**
315 To confirm cancer cell proliferation EDU staining was performed, as previously reported, larvae
316 were incubated in 10μM 5-ethynyl-2'deoxyuridiine (EdU) solution in E3 for 4 hours with gentle
317 rocking (9). Xenografts were then fixed in 4% PFA overnight at 4°C, washed in 1x PBS, and
318 stored in 100% methanol at -20°C. For the EDU staining, samples were rehydrated in a series of
319 methanol dilutions and permeabilized following the manufacturer instructions on Click-iT EdU
320 imaging kit (Life Technologies). Samples were stored in Vectashield (Vector Laboratories) and
321 then imaged at the Nikon CSU spinning disk confocal microscope. The number of EDU positive
322 cells were automatically counted in the larvae tumor area using IMARIS spots function (9).
323 Spots were defined as particles with 9.5 μm of X/Y and Z diameter (9). To quantify EDU positive
324 cells only in the tumor, a surface was created and then the EDU signal was masked to isolate
325 EDU positive cells in the tumor.
326
327 **Mass volume 3D rendering on IMARIS**
328 To quantify tumor volume and angiogenic infiltration, the larval tumor area was imaged as
329 previously described and reconstructed using IMARIS Bitplane Software (Version 9.9.1/10.1)
330 rendering mode. To quantify mass volume/area a 3D surface was generated using the
331 tdTomato fluorescent marker that the cancer cells express. All signal outside of the tumor

surface was then masked to isolate endothelial cells within the tumor (9). A second surface was then created for the endothelial cells.

Automatic quantification of PIP-FUCCI cancer cells on IMARIS

To quantify the total number of cancer cells and the tumor volume, the larval tumor area was imaged as previously described and reconstructed using IMARIS Bitplane Software (Version 9.9.1/10.1) rendering mode and the total number of cancer cells were automatically counted using IMARIS spots function. Spots were defined as particles with 9.5 μm diameter X/Y and Z and to quantify mass volume and area a surface for each region/area was created. For the PIP-FUCCI model the spots and surface function were created in both fluorescent channels. To quantify G2/M cells, that should be fluorescent in both channels, spots were defined as particles with less than 4 μm distance from spots in the opposite fluorescent channel.

Neutrophil quantification on IMARIS

To quantify neutrophil recruitment to the tumor area and neutrophil infiltration of the tumor, the larval tumor area was imaged as previously described and reconstructed using IMARIS Bitplane Software (Version 9.9.1/10.1) rendering mode and the total number of cancer cells were automatically counted using IMARIS spots function (10). All neutrophils in the FOV (field of view) were counted and neutrophils in the tumor were isolated and counted. Neutrophil density was calculated by normalizing the number of neutrophils per tumor volume.

Statistical Analysis

All experiments were replicated independently two to three times (N) with multiple samples in each replicate (n). For analysis of mass volume/area, vessel volume/area, and PIP-Fucci cell phases an unpaired Mann-Whitney T-test was performed on GraphPad Prism version 9.3 (10). For mass to vessel volume correlation a Pearson correlation was performed using GraphPad Prism version 9.3. All graphical representations were done on GraphPad Prism version 9.3.

References

1. Prasongsook N, Kumar A, Chintakuntlawar AV, Foote RL, Kasperbauer J, Molina J, et al. Survival in Response to Multimodal Therapy in Anaplastic Thyroid Cancer. The Journal of Clinical Endocrinology & Metabolism. 2017;102(12):4506-14.
2. Hason M, Bartůněk P. Zebrafish Models of Cancer-New Insights on Modeling Human Cancer in a Non-Mammalian Vertebrate. Genes (Basel). 2019;10(11).
3. Fior R, Póvoa V, Mendes RV, Carvalho T, Gomes A, Figueiredo N, et al. Single-cell functional and chemosensitive profiling of combinatorial colorectal therapy in zebrafish xenografts. Proceedings of the National Academy of Sciences. 2017;114(39):E8234-E43.
4. Rebelo de Almeida C, Mendes RV, Pezzarossa A, Gago J, Carvalho C, Alves A, et al. Zebrafish xenografts as a fast screening platform for bevacizumab cancer therapy. Communications Biology. 2020;3(1):299.
5. Veinotte CJ, Dellaire G, Berman JN. Hooking the big one: the potential of zebrafish xenotransplantation to reform cancer drug screening in the genomic era. Dis Model Mech. 2014;7(7):745-54.
6. Póvoa V, Rebelo de Almeida C, Maia-Gil M, Sobral D, Domingues M, Martinez-Lopez M, et al. Innate immune evasion revealed in a colorectal zebrafish xenograft model. Nature Communications. 2021;12(1):1156.
7. Pan Z, Xu T, Bao L, Hu X, Jin T, Chen J, et al. CREB3L1 promotes tumor growth and metastasis of anaplastic thyroid carcinoma by remodeling the tumor microenvironment. Molecular Cancer. 2022;21(1):190.
8. Au - Martinez-Lopez M, Au - Póvoa V, Au - Fior R. Generation of Zebrafish Larval Xenografts and Tumor Behavior Analysis. JoVE. 2021(172):e62373.
9. de Oliveira S, Houseright RA, Graves AL, Golenberg N, Korte BG, Miskolci V, et al. Metformin modulates innate immune-mediated inflammation and early progression of NAFLD-associated hepatocellular carcinoma in zebrafish. Journal of hepatology. 2019;70(4):710-21.
10. Feliz-Norberto M, Michael C, de Oliveira S. Neutrophil reverse migration from liver fuels neutrophilic inflammation to tissue injury in Nonalcoholic Steatohepatitis. bioRxiv. 2021:2021.10.03.462893.
11. Xu B, Fuchs T, Dogan S, Landa I, Katabi N, Fagin JA, et al. Dissecting Anaplastic Thyroid Carcinoma: A Comprehensive Clinical, Histologic, Immunophenotypic, and Molecular Study of 360 Cases. Thyroid. 2020;30(10):1505-17.
12. Hanahan D, Weinberg Robert A. Hallmarks of Cancer: The Next Generation. Cell. 2011;144(5):646-74.
13. Lawson ND, Weinstein BM. In vivo imaging of embryonic vascular development using transgenic zebrafish. Dev Biol. 2002;248(2):307-18.
14. Grant GD, Kedziora KM, Limas JC, Cook JG, Purvis JE. Accurate delineation of cell cycle phase transitions in living cells with PIP-FUCCI. Cell Cycle. 2018;17(21-22):2496-516.
15. Wong K, Di Cristofano F, Ranieri M, De Martino D, Di Cristofano A. PI3K/mTOR inhibition potentiates and extends palbociclib activity in anaplastic thyroid cancer. Endocr Relat Cancer. 2019;26(4):425-36.
16. Park JT, Leach SD. Zebrafish model of KRAS-initiated pancreatic cancer. Anim Cells Syst (Seoul). 2018;22(6):353-9.

17. Kirchberger S, Sturtzel C, Pascoal S, Distel M. Quo natas, Danio?-Recent Progress in Modeling Cancer in Zebrafish. Front Oncol. 2017;7:186.
18. Zuazo-Gaztelu I, Casanovas O. Unraveling the Role of Angiogenesis in Cancer Ecosystems. Frontiers in Oncology. 2018;8.
19. Gabellini C, Gómez-Abenza E, Ibáñez-Molero S, Tupone MG, Pérez-Oliva AB, de Oliveira S, et al. Interleukin 8 mediates bcl-xL-induced enhancement of human melanoma cell dissemination and angiogenesis in a zebrafish xenograft model. International Journal of Cancer. 2018;142(3):584-96.
20. Bauerle KT, Schweppe RE, Lund G, Kotnis G, Deep G, Agarwal R, et al. Nuclear factor κB-dependent regulation of angiogenesis, and metastasis in an in vivo model of thyroid cancer is associated with secreted interleukin-8. J Clin Endocrinol Metab. 2014;99(8):E1436-44.
21. Galdiero MR, Varricchi G, Loffredo S, Bellevicine C, Lansione T, Ferrara AL, et al. Potential involvement of neutrophils in human thyroid cancer. PLOS ONE. 2018;13(6):e0199740.
22. Szczerba BM, Castro-Giner F, Vetter M, Krol I, Gkountela S, Landin J, et al. Neutrophils escort circulating tumour cells to enable cell cycle progression. Nature. 2019;566(7745):553-7.

Competing interests: The authors declare no competing interests.

Authors Contribution: CM, ADC and SDO conceived and designed experiments. CM performed experiments. CM performed data analysis. CM and SdO wrote the manuscript. SDO and ADC critically reviewed and edited the manuscript; All authors reviewed and approved the manuscript.

Grant Support: SdO supported by R35 GM118027 and ADC supported by CA128943.

Acknowledgments: We want to thank Rita Fior for the helpful discussions and all the support and technical advice given during the development of this work. We thank the Zebrafish core facility, Clint Depaolo and Spartak Kalinin, and the Analytical Imaging Facility (AIF), of Albert Einstein College of Medicine. The AIF is funded by the NCI (P30CA013330).

Table 1.

Cell Line	Species of origin	Mutations	Culture Medium
N794	Mouse	*Nras*^{Q61R}, *Pten*$^{-/-}$, *Tp53*$^{-/-}$	DMEM
T4888M	Mouse	*Pten*$^{-/-}$, *Tp53*$^{-/-}$	DMEM
T1903	Mouse	*Pten*$^{-/-}$, *Tp53*$^{-/-}$	DMEM
T1860	Mouse	*Pten*$^{-/-}$, *Tp53*$^{-/-}$	DMEM
N2773	Mouse	*Nras*^{Q61R}, *Pten*$^{-/-}$, *Tp53*$^{-/-}$	DMEM
N2933	Mouse	*PIK3CA*^{H1047R}, *Pten*$^{-/-}$, *Tp53*$^{-/-}$	DMEM
BHT101	Human	*BRAF*^{V600E}, *TP53*^{I251T}	RPMI
CAL62	Human	*KRAS*^{G12R}, *TP53*^{A161D}	DMEM
C643	Human	*HRAS*^{G13R}, *TP53*^{R248Q}	RPMI
OCUT2	Human	*PIK3CA*^{H1047R}, *BRAF*^{V600E}	RPMI
ACT1	Human	*NRAS*^{Q61K}, *TP53*^{C242S}	DMEM
ASH3	Human	*PTEN*^{F241fs}, *NRAS*^{Q61R}, *Tp53*^{H179R}	RPMI
SW1736	Human	*BRAF*^{V600E}, *TP53*^{Q193*}	RPMI

Figure 1. ATC cell lines engraft in zebrafish larvae at different rates.

(A) Experimental timeline for thyroid xenotransplant model. (B) Representative images acquired using the stereomicroscope at 2 dpf to show proper site of injection. (C) Graph showing percent engraftment for ATC mouse (N794, T1903, T1860, N2773, N2933, T4888M) and human (ACT1, BHT101, ASH3, C643) cell lines. (D) Representative images acquired using the fluorescent microscope at 4 dpi in mouse and human ATC cell lines. Scale bar= 100 μm (E-G & J-L) Representative images of T4888 and C643 ATC cell lines in zebrafish. Scale bar= 20 μm. (E'-G' & J'-L') Higher magnification showcasing important histopathological features maintained in T4888 and C643 ATC zebrafish xenotransplants. Scale bar= 20 μm. (H & H') Histopathological analysis from original lung metastasis of T4888 ATC cells in a murine mouse model ((Pten, P53)/-/-). Scale bar= 50 μm. (I & I') Histopathological analysis from an allograft in a murine mouse model. Scale bar= 50 μm. Data is from at least two independent experimental replicates. Bar plots show mean ± SEM, each dot represents one experiment.

Figure 2. T4888M and C643 ATC cell lines display different growth and proliferation rates.

(A) Graph showing mass volume μm^3 at 1 dpi compared to 4 dpi in ATC cell lines T4888 and C643 (T4888 n=26, C643 n=27). (B) Graph showing mass volume μm^3 at 1 dpi compared to 4 dpi tracking individual larva in ATC cell lines T4888 and C643. (C-D) Representative 3D images and reconstruction of ATC tumor masses from 1 dpi to 4 dpi in ATC cell lines T4888 and C643. Images were acquired using the 20x objective. Scale bar= 50 μm. (E) Representative 3D images of EDU+ cells inside cancer mass of ATC cell lines T4888 and C643. (F) Quantification of the total number of EDU+ cells in T4888 and C643 ATC masses (T4888 n=15, C643 n=16). Images were acquired using the 40x objective. Scale bar= 30 μm. (G) Quantification of the number of EDU+ cells normalized by the area μm^2 of the ATC mass. Data is from at least two independent experimental replicates. Bar plots show mean ± SEM, each dot represents one larva, P-values are shown in each graph.

Figure 3. T4888M ATC xenotransplants display high angiogenic ability.

(A-B) Representative 3D images of ATC tumor mass and vessel recruitment at 4 dpi Tg(fli:GFP) in ATC cell lines T4888 and C643. Scale bar= 50 μm. (C) Graph showing vessel density in tumor mass normalized by tumor volume μm^3 for ATC cell lines T4888 and C643 (T4888 n=26, C643 n=26). (D) Graph showing vessel density in tumor mass normalized by tumor area μm^2 for ATC cell lines T4888 and C643 (T4888 n=26, C643 n=26). (E) Graph of the correlation between T4888 mass volume and T4888 vessel volume. (F) Graph of the correlation between C643 mass volume and C643 vessel volume (T4888 n=26, C643 n=26). Data is from at least two independent experimental replicates. Bar plots show mean ± SEM, each dot represents one larva, P-values are shown in each graph. Pearson correlation graphs show line of best fit; each dot represents one larva, r-values are shown in each graph.

Figure 4. In vivo visualization of T4888M cell cycle using the PIP-FUCCI reporter.

(A) Representative 3D images of T4888 ATC cancer cells using the PIP-FUCCI reporter. Scale bar= 30 μm. (B) Graph showing total number of cells at 4 dpi in each cell cycle phase with the PIP-FUCCI reporter (T4888 n=22). (C) Graph showing cell cycle phases with the PIP-FUCCI reporter normalized by the total number of cells in T4888 ATC mass (T4888 n=22). (D-E) Images from 48-hour live imaging to highlight proliferative cells, imaging begins 24 hpi and ends at 72 hpi. Data is from at least two independent experimental replicates. Bar plots show mean ± SEM, each dot represents one larva, P-values are shown in each graph.

Figure 5. T4888M ATC cell line responds to cell cycle inhibitors.

(A-C) Representative 3D images of ATC tumor mass and neutrophil recruitment at 4 dpi Tg(lyzC:BFP) with DMSO control and AZD2014 treatment. Zebrafish larvae were treated with 0/1% DMSO control or 1 μm AZD2014 (Vistusertib). Scale bar= 20 μm. (D) Graph showing cell cycle phases with the PIP-FUCCI reporter normalized by the total number of cells in DMSO control and AZD2014 treatment (DMSO Control n=14, AZD2014 n=22). (E) Graph showing total number of cells in each mass in DMSO control and AZD2014 treatment (DMSO Control n=14, AZD2014 n=22). (F) Graph showing the total number of neutrophils in field of view (FOV) for the DMSO control and AZD2014 (DMSO Control n=14, AZD2014 n=18). (G) Graph showing total number of neutrophils infiltrating the mass in the DMSO control and AZD2014 (DMSO Control

n=14, AZD2014 n=18). (H) Graph showing the total number neutrophils normalized by the total number of cells in each larva (DMSO Control n=14, AZD2014 n=18). Data is from at least two independent experimental replicates. Bar plots show mean ± SEM, each dot represents one larva, P-values are shown in each graph.

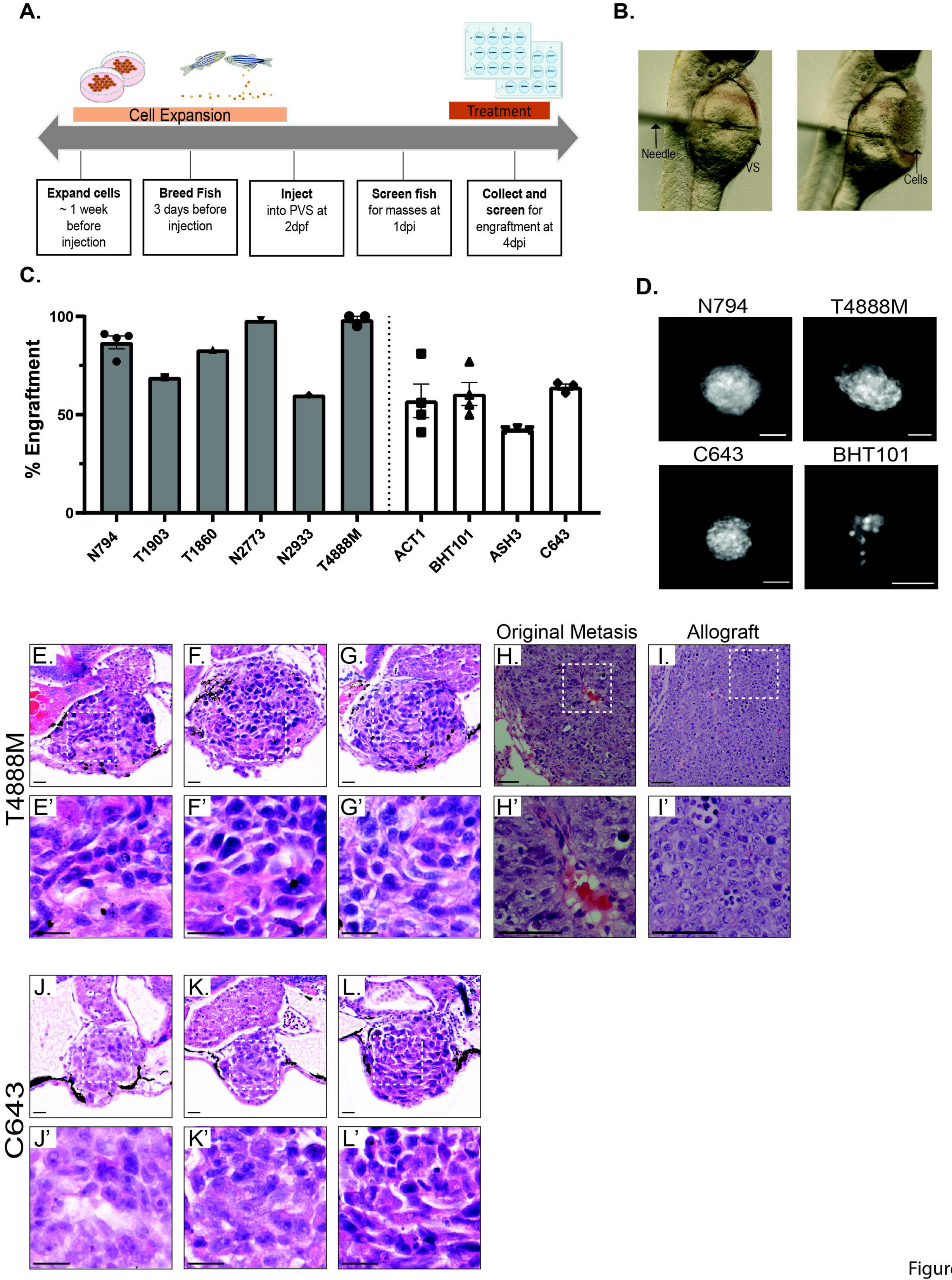
A.
Cell Expansion
Treatment
Expand cells ~ 1 week before injection
Breed Fish 3 days before injection
Inject into PVS at 2dpf
Screen fish for masses at 1dpi
Collect and screen for engraftment at 4dpi
B.
Needle
VS
Cells
C.
% Engraftment
100
50
0
N794
T1903
T1860
N2773
N2933
T4888M
ACT1
BHT101
ASH3
C643
D.
N794
T4888M
C643
BHT101
Original Metasis
Allograft
T4888M
C643
E.
F.
G.
H.
I.
E'
F'
G'
H'
I'
J.
K.
L.
J'
K'
L'

Figure 1

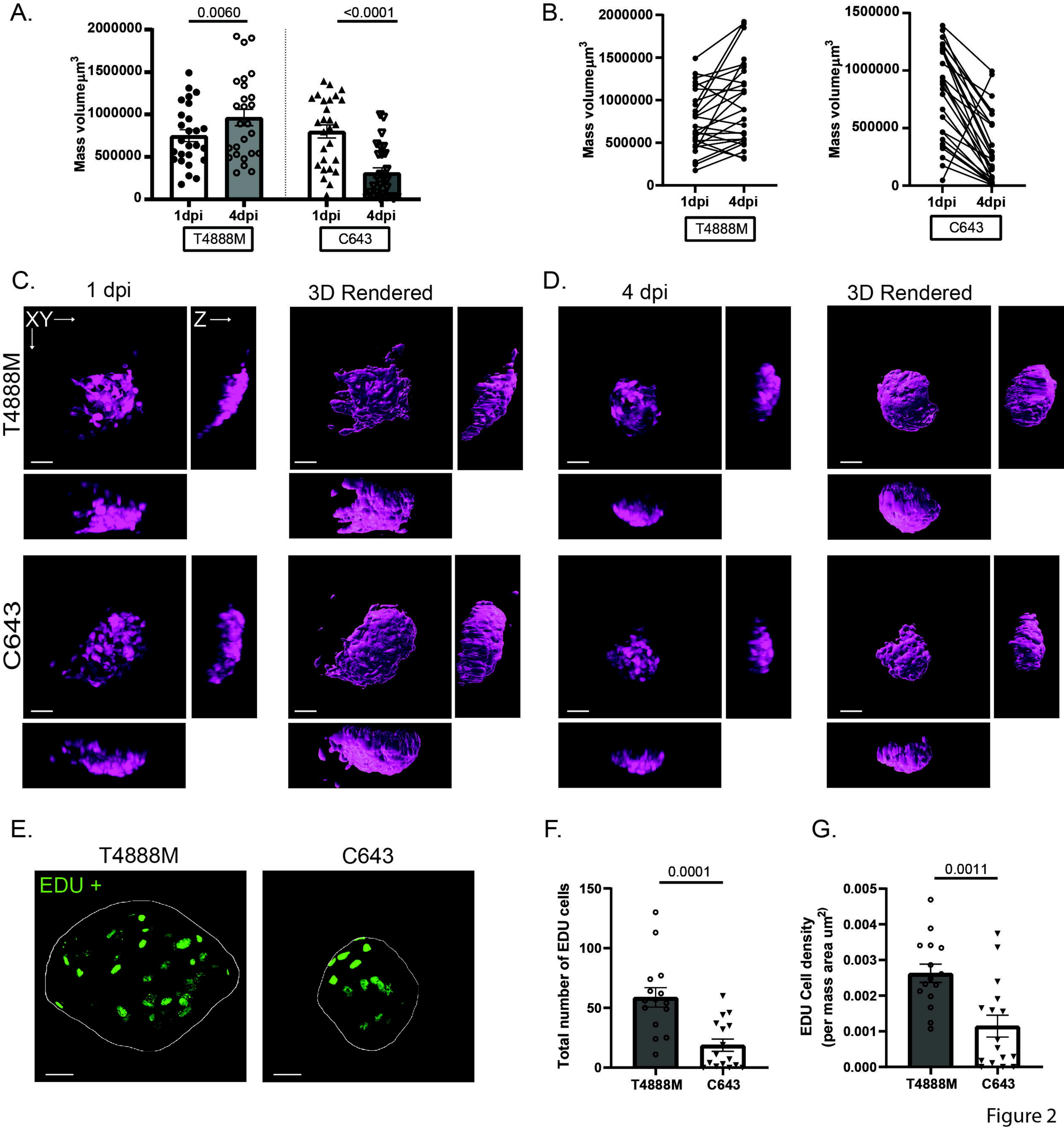
A.
0.0060
<0.0001
Mass volumeμm3
2000000
1500000
1000000
500000
0
1dpi
4dpi
1dpi
4dpi
T4888M
C643
B.
Mass volumeμm3
2000000
1500000
1000000
500000
0
1dpi
4dpi
T4888M
Mass volumeμm3
1500000
1000000
500000
0
1dpi
4dpi
C643
C.
1 dpi
3D Rendered
XY→
Z→
T4888M
C643
D.
4 dpi
3D Rendered
E.
T4888M
C643
EDU +
F.
0.0001
Total number of EDU cells
150
100
50
0
T4888M
C643
G.
0.0011
EDU Cell density
(per mass area um2)
0.005
0.004
0.003
0.002
0.001
0.000
T4888M
C643

Figure 2

A.

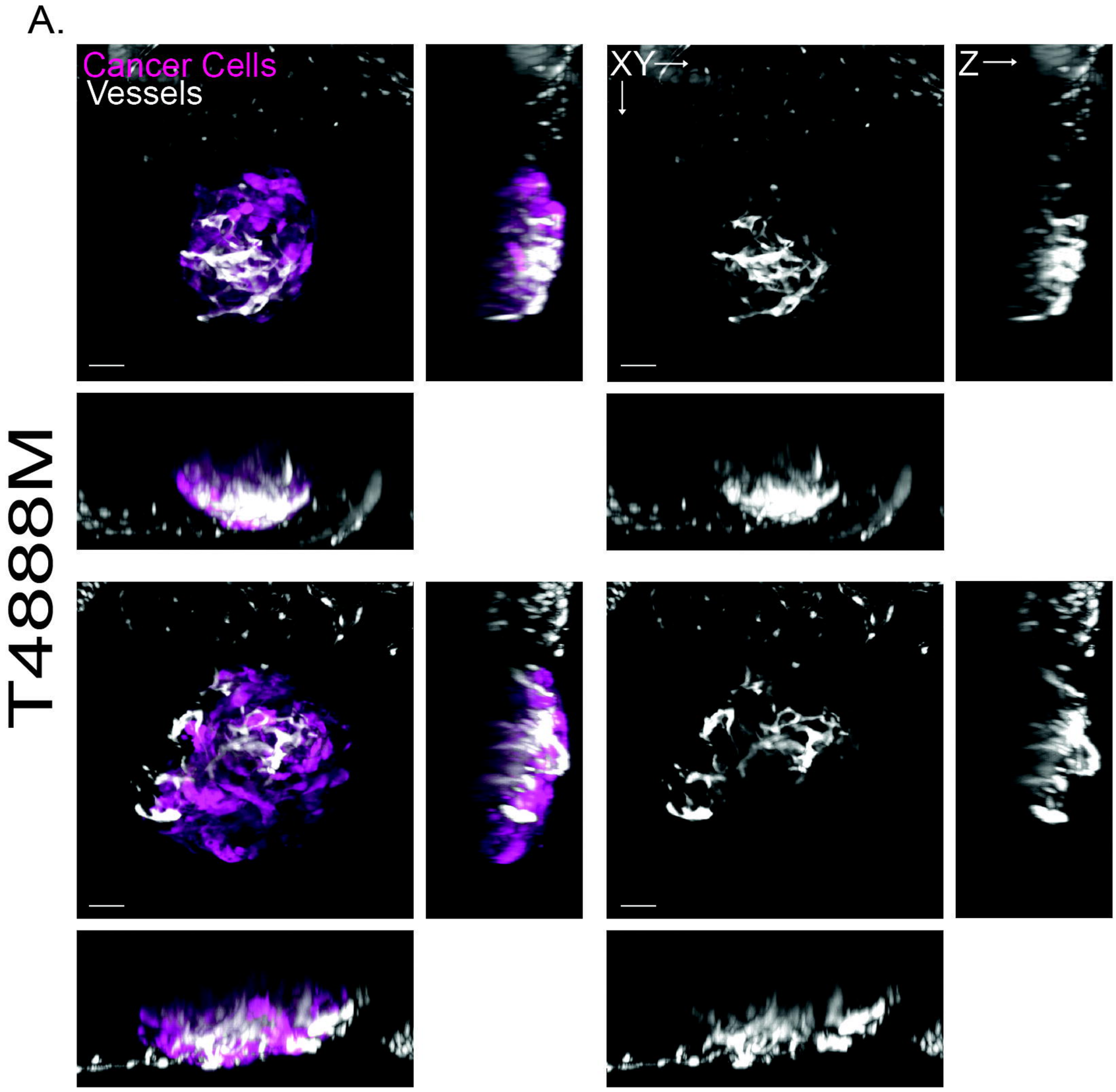

B.

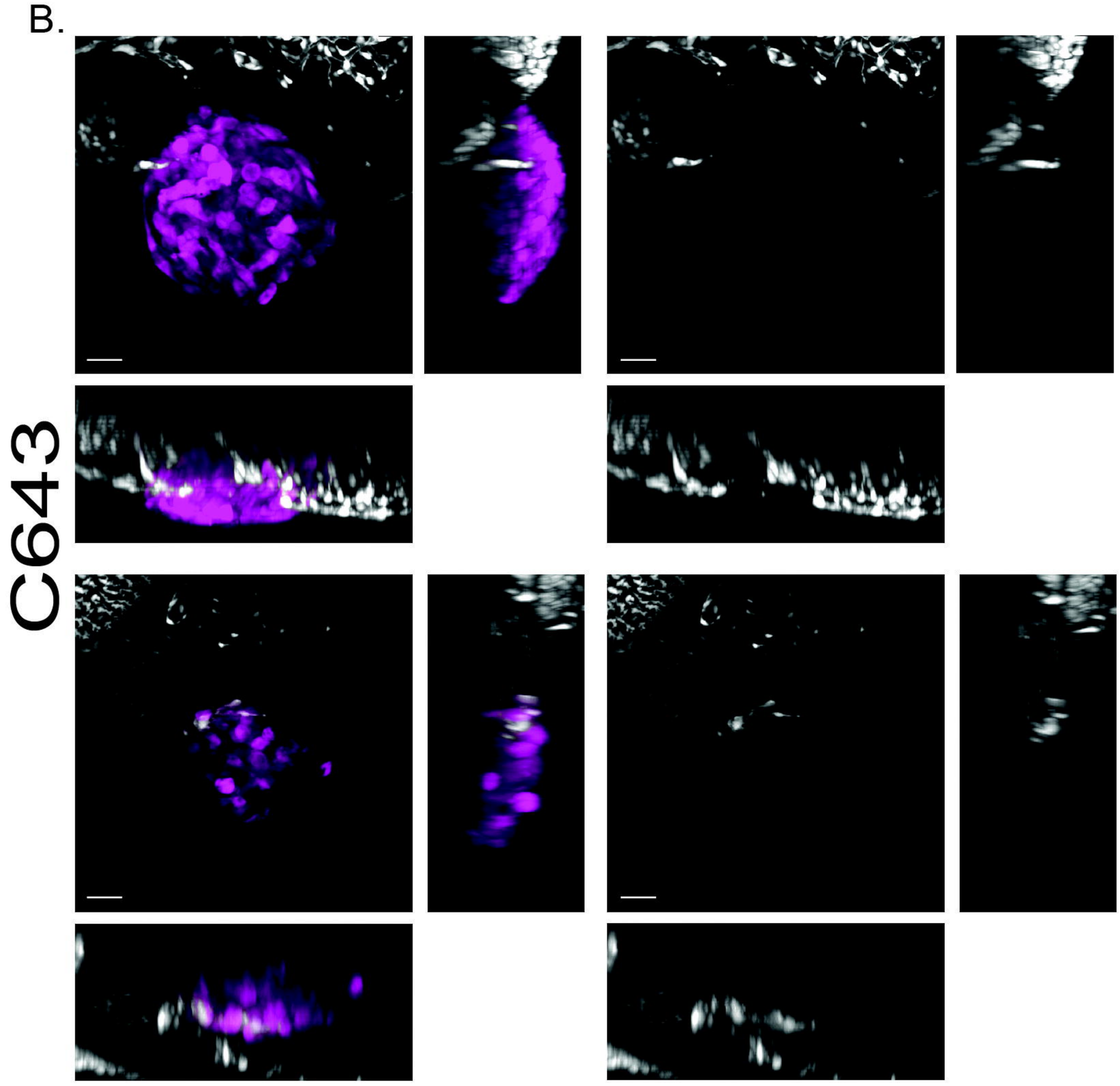

C.

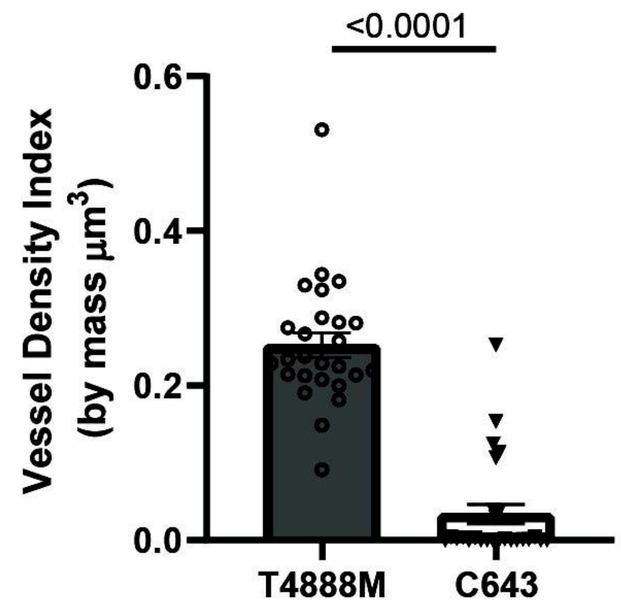

D.

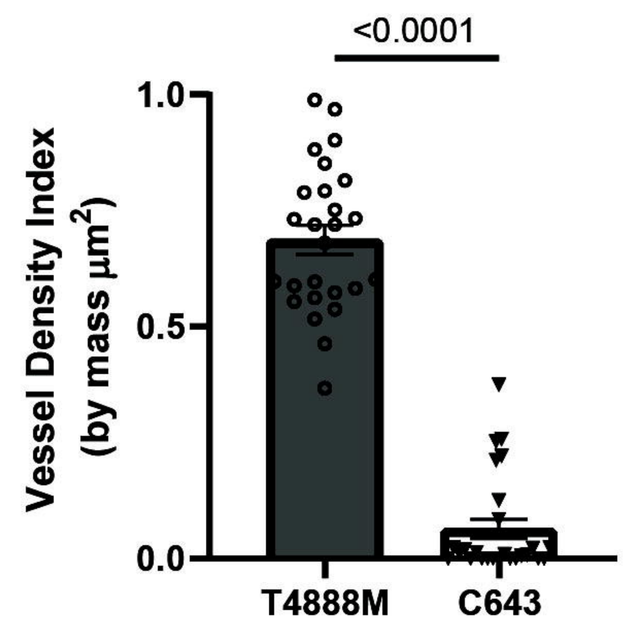

E.

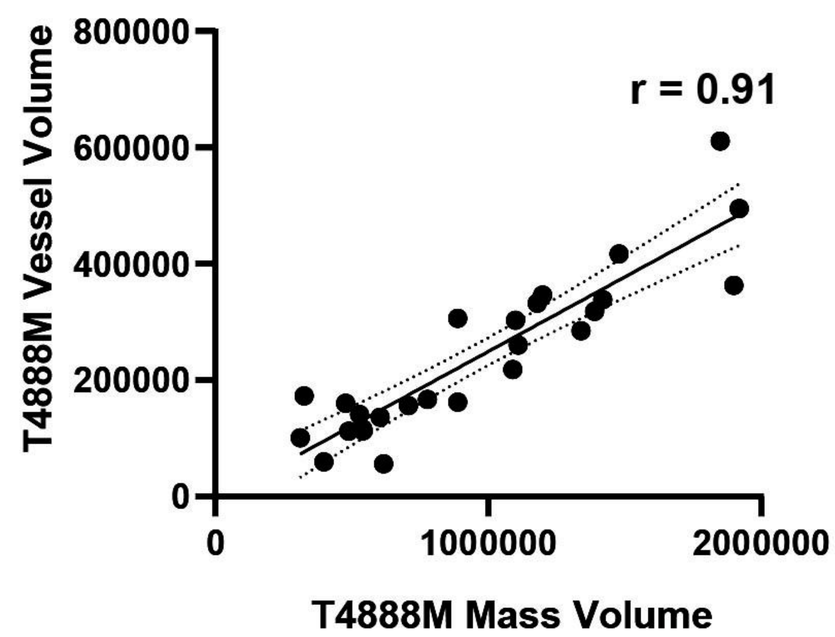

F.

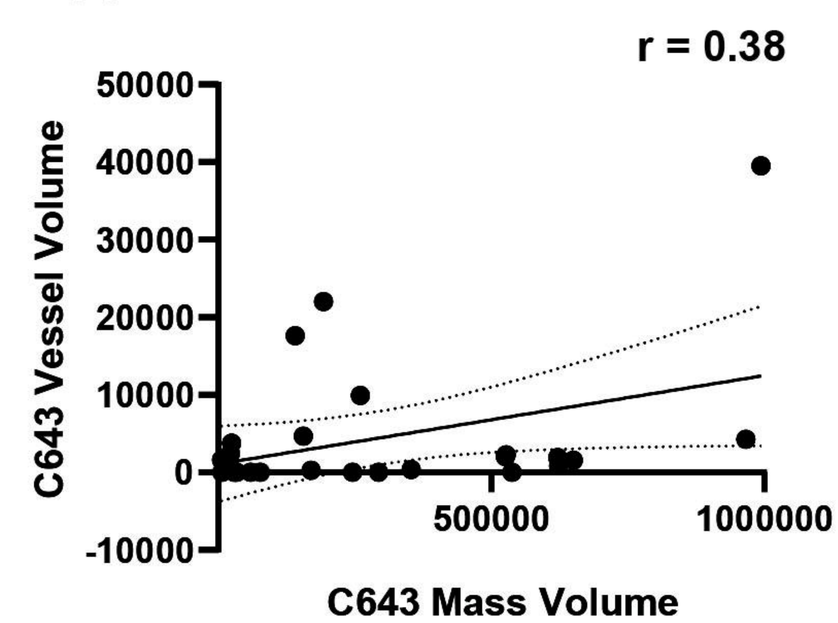

Figure 3

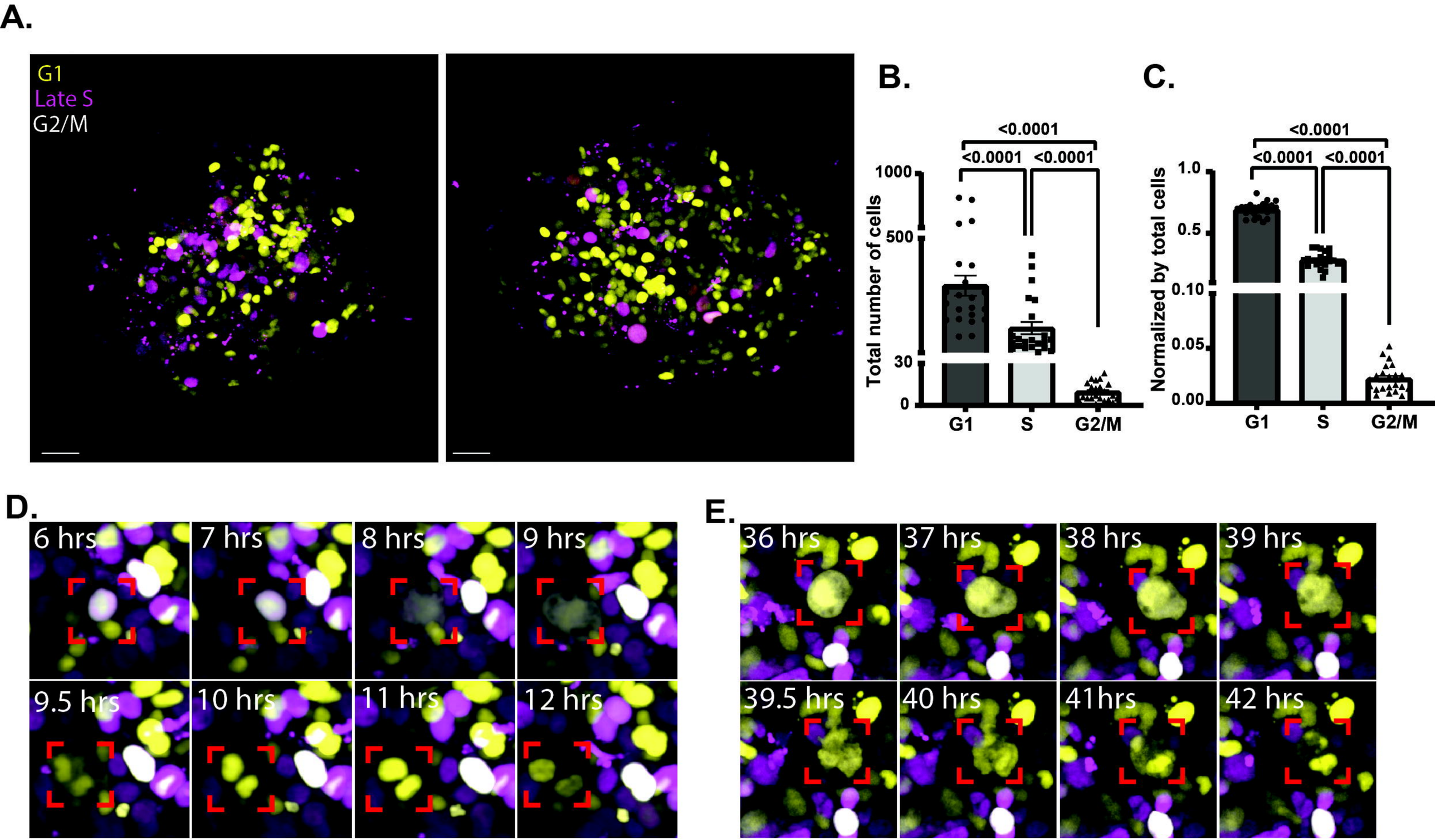
A.
G1
Late S
G2/M
B.
<0.0001
<0.0001
<0.0001
Total number of cells
1000
500
30
0
G1
S
G2/M
C.
<0.0001
<0.0001
<0.0001
Normalized by total cells
1.0
0.5
0.10
0.05
0.00
G1
S
G2/M
D.
6 hrs
7 hrs
8 hrs
9 hrs
9.5 hrs
10 hrs
11 hrs
12 hrs
E.
36 hrs
37 hrs
38 hrs
39 hrs
39.5 hrs
40 hrs
41hrs
42 hrs

Figure 4

A.

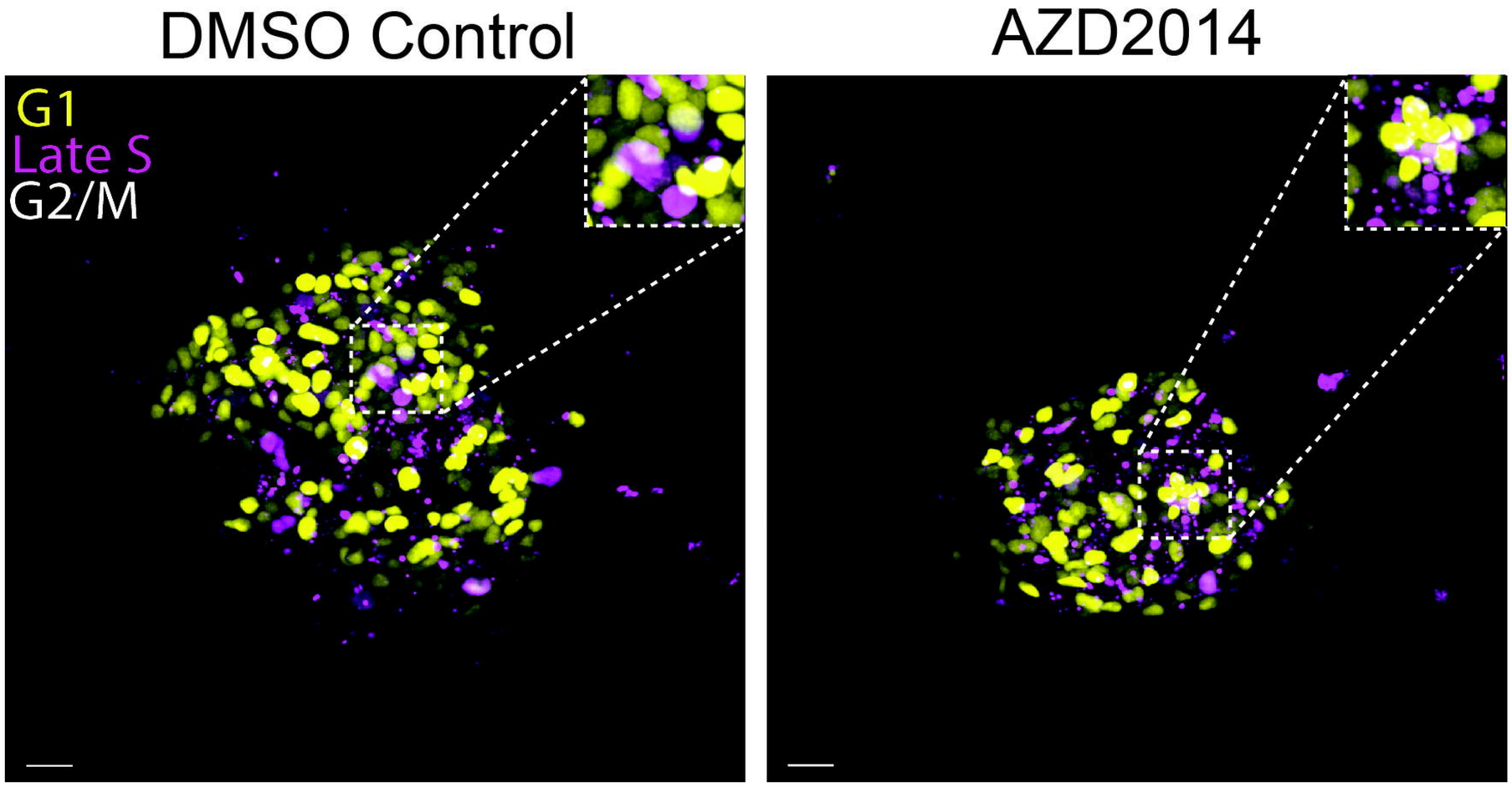

B.

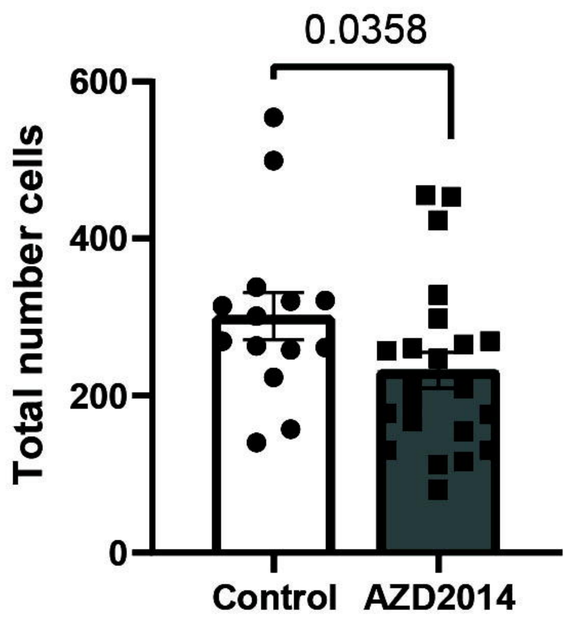

C.

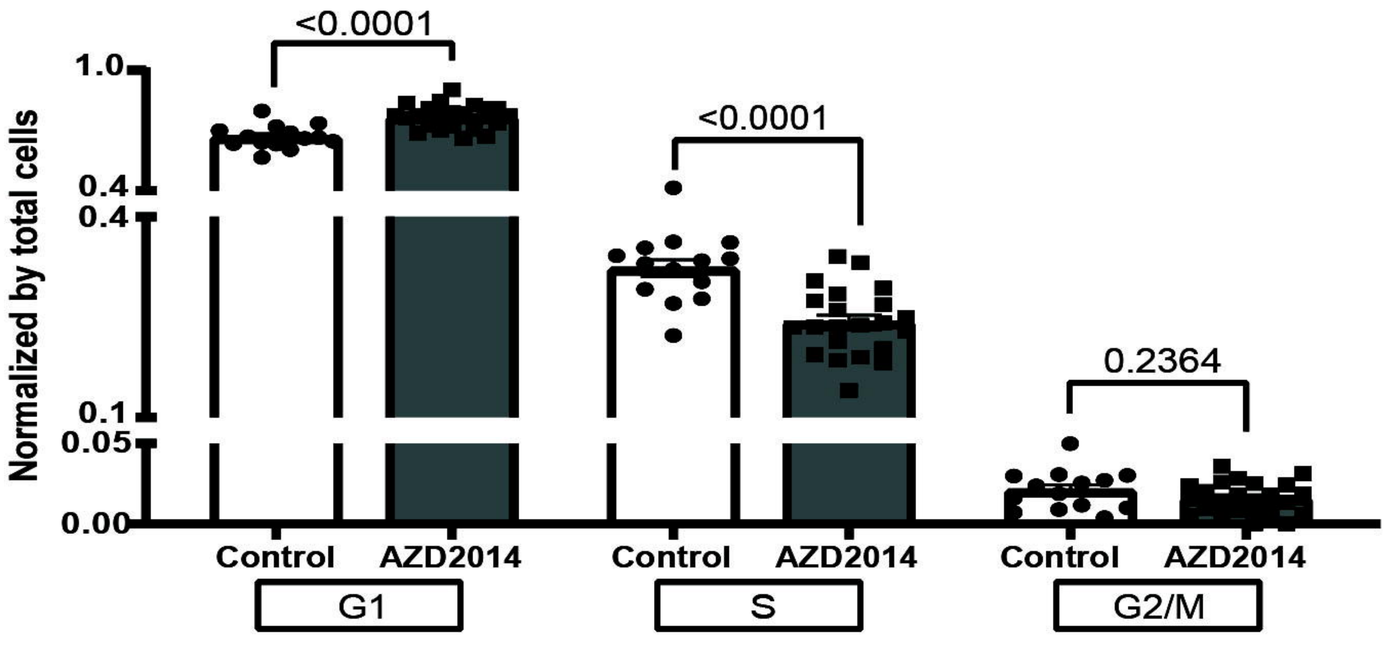

F.

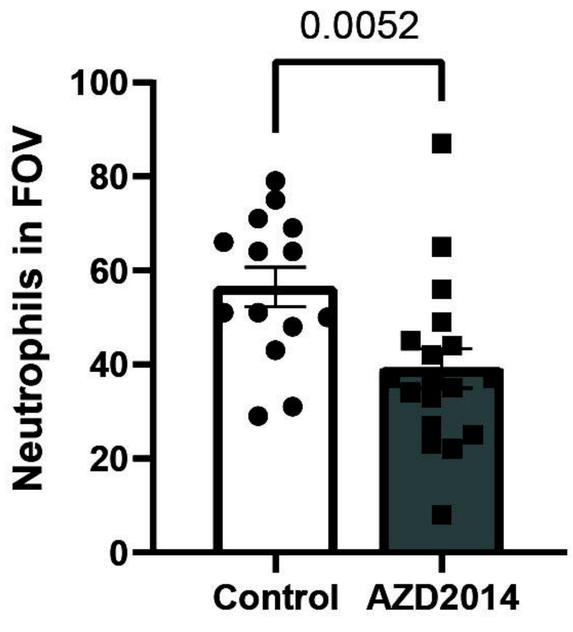

D.

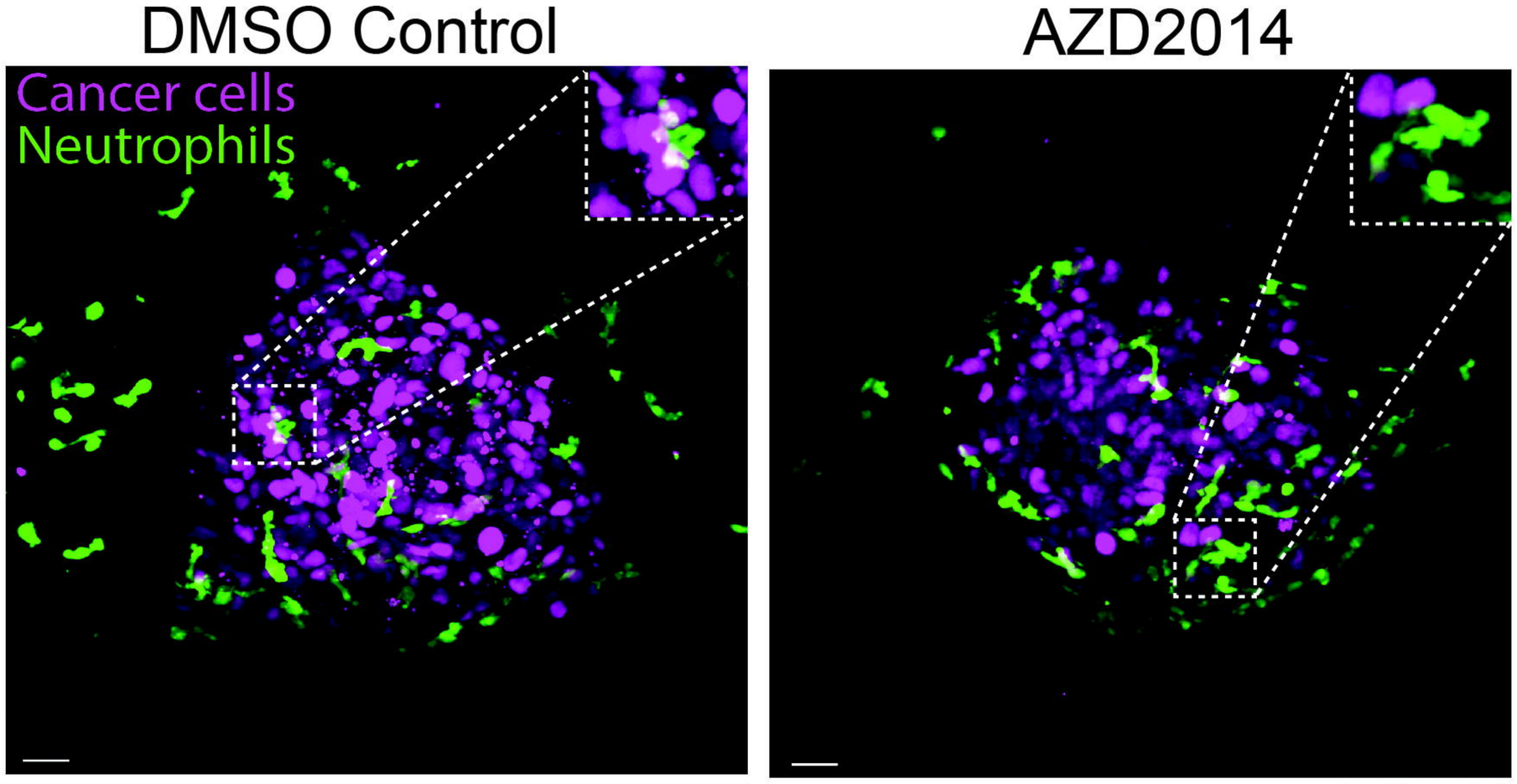

G.

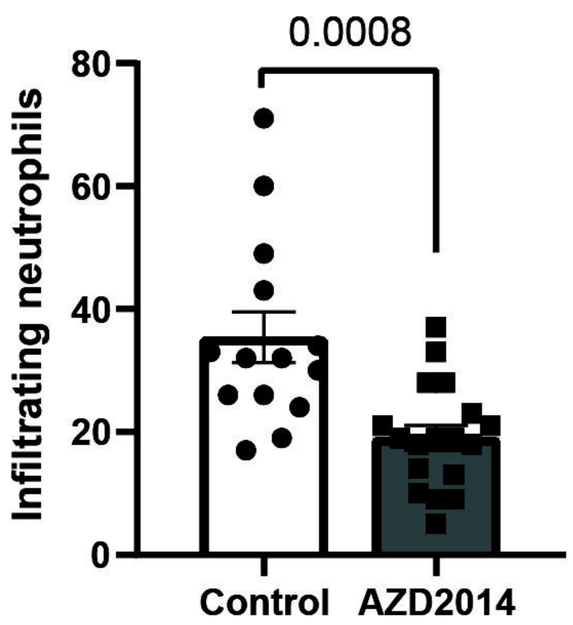

E.

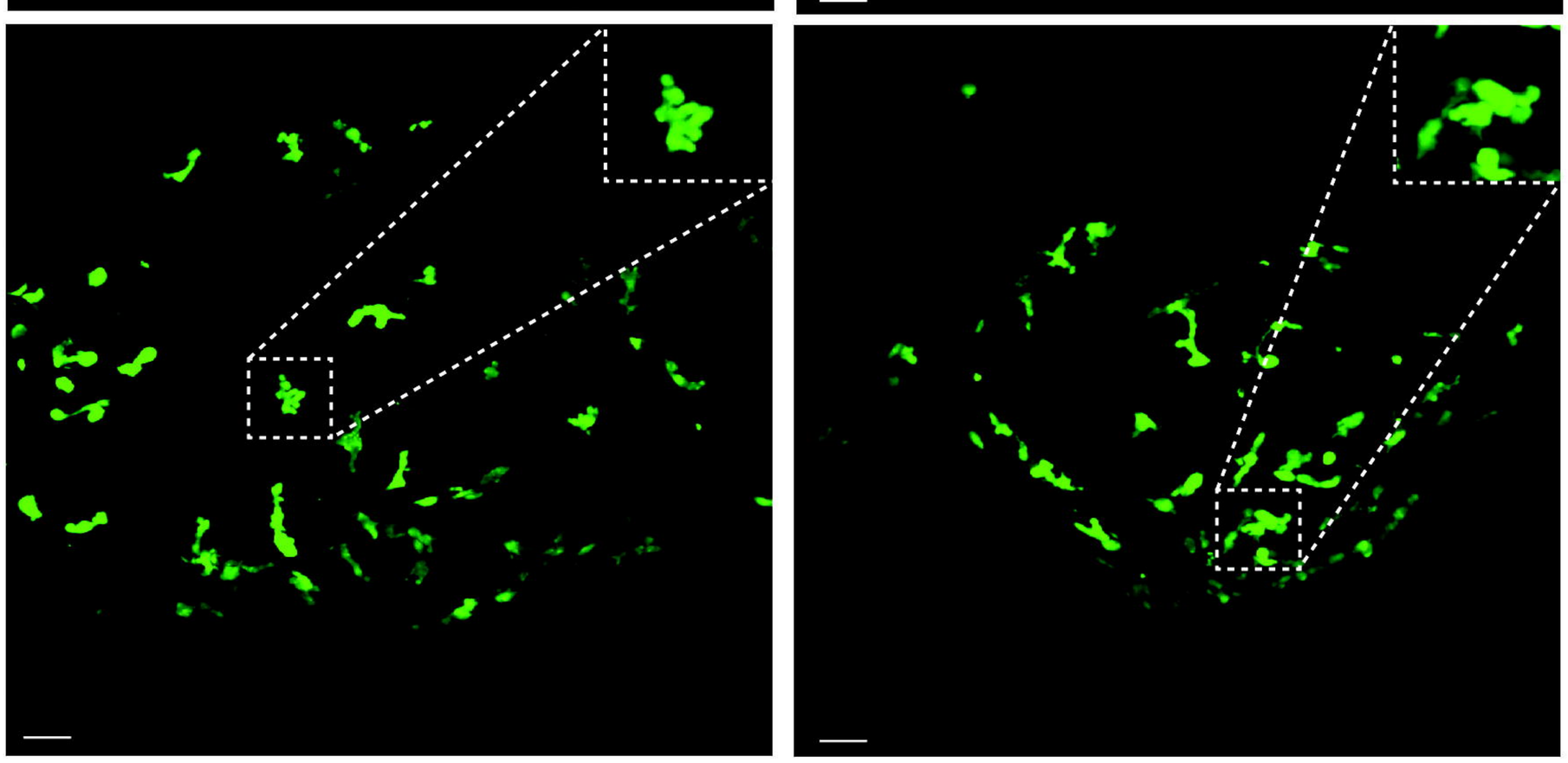

H.

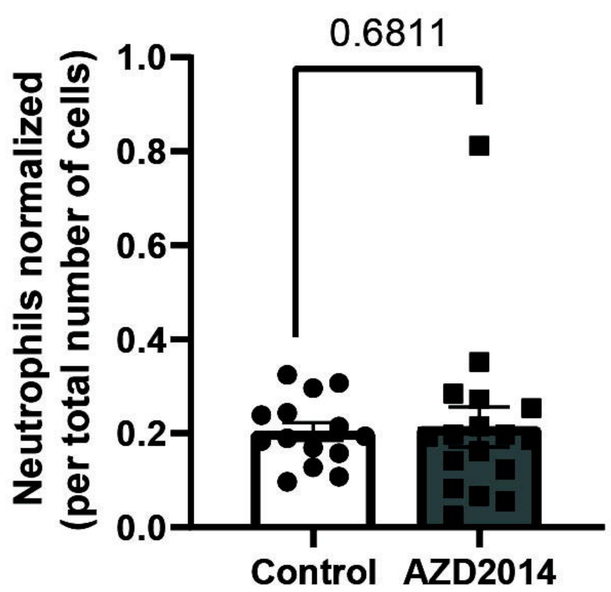

Figure 5